Master's thesis

NTNU
Norwegian University of Science and Technology
Faculty of Natural Sciences
Department of Physics

Ørjan Åvitsland

Optimising ultrasonic beamforming through solid plates

Master's thesis in Applied Physics and Mathematics
Supervisor: Erlend Magnus Viggen
Co-supervisor: Ingve Simonsen
June 2021

NTNU
Norwegian University of
Science and Technology

Ørjan Åvitsland

Optimising ultrasonic beamforming through solid plates

Master's thesis in Applied Physics and Mathematics
Supervisor: Erlend Magnus Viggen
Co-supervisor: Ingve Simonsen
June 2021

Norwegian University of Science and Technology
Faculty of Natural Sciences
Department of Physics

NTNU
Norwegian University of
Science and Technology

Abstract

Ultrasonic tools provide a non-destructive way of to test the integrity of the cement sheath surrounding boreholes. Commonly used tools do not make use of dynamic focusing, and are therefore limited in the information they can give. Focusing the ultrasound beam at varying depths in the material can provide better imaging of the volume surrounding the borehole. A major challenge lies in the difficulty of achieving good focusing through the steel and transmitting enough energy, as the impedance differences are high.

A numerical method of rapidly testing and characterizing different beamforming methods is developed, by making use of the superposition principle of waves. The procedure is split into a simulation stage and a post-processing stage. In the first stage, the wave field emitted from a single transducer element is computed numerically by the 2D finite-difference time-domain (FDTD) simulation software SimSonic. In the post-processing stage, this wave field can be shifted both in time and space, and then superimposed onto itself to build up a fully controllable transducer array. This allows for rapid testing of a wide range of beamforming parameters. Several techniques of focusing are tested in search of the most suitable method of focusing through solid plates. The effect of an apodisation window on the transducer is explored. A benefit in using shear-wave based focusing methods is found, at an azimuth between 24 mm and 40 mm for this setup.

Sammendrag

Ultrasoniske verktøy gir en ikke-destruktiv måte å teste integriteten av borehull og sementen som ligger rundt røret. Dagens verktøy tar ikke i bruk dynamisk fokusering, og visse begrensninger på grunn av dette. Å fokusere ultralydstråler på varierende dybder i materialet kan gi bedre avbildning av hele volumet rundt borehullet. En stor utfordring ligger i vanskeligheten ved å oppnå god fokusering gjennom stålrøret, som introduserer mye støy på grunn av interne refleksjoner i stålet, i tillegg til å store impedanseforskjeller mellom vannet og stålet.

En numerisk metode for å raskt teste og karakterisere ulike fokuseringsmetoder er utviklet, ved å ta i bruk superposisjonsprinsippet for bølger. Prosedyren er delt opp i en simuleringsfase og en etterbehandlingsfase. I den første fasen blir bølgefeltet fra ett enkelt transducerelement simulert numerisk i programvaren SimSonic, som løser 2D elastodynamiske ligninger. Dette bølgefeltet er lagret som en funksjon av posisjon og tid, og kan superposisjoneres på seg selv med ulike tidsforskyvelser for å bygge opp en fullstending og kontrollerbar transducer. Dette tillater hurtig testing av ulike parametere for stråleforming. Flere teknikker utprøves for å undersøke hvilke av disse som er best egnet for å fokusere gjennom stålplater. Effekten av et apodiseringsvindu undersøkes. Fordelen ved å bruke en skjærbølge-basert fokusering oppdages, og god fokusering med lite støy oppnås ved azimut mellom 24 mm og 40 mm for dette oppsettet.

Preface

I would like to extend my thanks to my supervisor Erlend Magnus Viggen at NTNU/CIUS, for useful insight and interesting discussions about acoustic well logging, as well as helpful feedback on the project work. I would also like to thank Andreas Talberg for giving an introduction to the SimSonic software, and providing Matlab code to serve as a starting point for the project.

Parts of the introduction, theory, and method description are adapted from an earlier project.

Contents

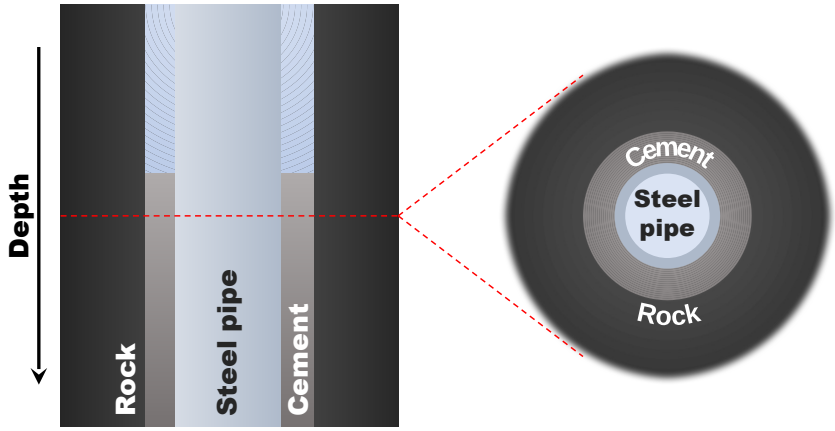

Figure 1: A sketch of the geometry of an oil well, where a steel pipe is encased by a layer of cement. *Adapted from a figure by Erlend Magnus Viggen.*

1 Introduction

1.1 Applications

Ultrasound technology sees a wide range of use in both medical and industrial applications. Industrially, ultrasound is commonly used in non-destructive testing of materials to detect internal flaws. In the oil industry, oil wells are typically sealed through the process of cementing to prevent fluids flowing into unwanted areas, as sketched in Figure 1. It is important that the cement provides a good seal around the pipe, and is free of defects. This can be difficult to achieve, and a structural failure will have large consequences for the companies responsible. The role of ultrasound technology lies in testing the integrity of this cement sheath. In short, ultrasound can be used to collect information about the impedance of the material begin the steel pipe. This data can then be analyzed to detect flaws in the cement sheath [1].

1.2 Common ultrasound methods in the industry

1.2.1 Pulse-echo tools

With pulse-echo tools, one single transducer surface emits a pulse directly towards the pipe, and then receives the echo [2, 3, 4]. The tool may rotate, giving information about the quality of the cement bond around the circum-

ference of the pipe at each depth. The pulse travels through the steel pipe, and is reflected at the back, on the steel-cement boundary. The time delay of the echo provides information on the thickness of the pipe, and the amplitude provides information about impedance of the material behind the pipe. If the cement is bonded well to the pipe, more energy is transmitted through to the cement, and less energy will be reflected back to the transducer. A poor bond gives instead a high impedance difference at the boundary, which results in more energy being reflected back.

1.2.2 Pitch-catch tools

A pitch-catch tool is typically separated into a transmitter and two receivers. The transmitter sends a pulse that travels along the direction of the pipe. As the pulse travels, waves are generated and radiated out on both sides of the pipe. This radiated signal is picked up by the two receivers, such that the rate of attenuation in the pulse can be measured. This gives information about the impedance behind the pipe. Combining this with a pulse-echo tool can reduce ambiguity in the material evaluation [5].

1.3 Motivation

The methods discussed so far are limited in that they only provide information about the cement immediately adjacent to the pipe. The quality of the steel-cement bonding does not tell the full story; there may be defects and channels deeper in the cement layer, which would go undetected. One common characteristic is that the methods all use a single transducer surface, and therefore lack any form of dynamic focusing.

Talberg *et al.* [6] researched the possibility of improving these techniques, through the use of a focused transducer array. Focusing the pulse at specific depths could provide more information about the integrity of the cement deeper into the layer. One challenge lies in achieving good target focusing, such that as much energy as possible reaches the desired target, with as little noise as possible. The existence of a solid plate makes it difficult to achieve a good focus, as interactions from shear waves and pressure waves in the

metal complicates the wave field. Talberg also investigated the possibility of operating above the critical angle of pressure waves in order to avoid some of these interactions.

This project seeks to overcome the challenge of focusing by taking advantage of the superposition principle of waves to efficiently compare methods for determining optimal beamforming, as well as investigating the effect of focusing at different angles.

The work is organised as follows. Firstly, the necessary theory behind ultrasound beamforming and the simulated annealing optimisation algorithm is presented. Then the method of using superposition in a post-processing step is outlined. All methods of focusing are then described. Lastly, all methods of focusing are compared in a large region below the steel plate.

2 Theory

2.1 Ultrasound beamforming

Ultrasound beamforming is the problem of controlling the interference pattern of waves, in order to shape and focus a pulse to the desired direction. In phased array ultrasonics, a transducer normally consists of a set of independently controlled elements that each emit a sound wave [7]. The interference of the waves from each element combine, and form a common beam through superposition. Controlling the phase and amplitude of the signal going to each element allows for steering and focusing of the beam, as sketched in Figure 2. Adding a linear delay to the elements introduces a deflection in the combined wave front, and allows for steering of the beam. Similarly, the beam can also be focused towards a point. This is done by considering the distance from each element to the desired focus point, and calculating how long time it will take for the wave to reach it from each element. This is simply given by the equation

$$\Delta t_i = \frac{r_i}{c} \tag{1}$$

where r_i measures the distance from each element on the transducer to the focal point, and c is the speed of sound in the medium. These delays have

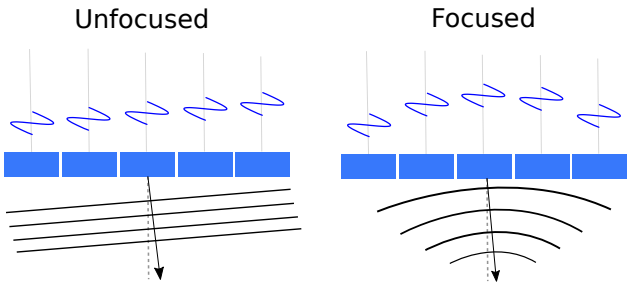

Figure 2: A sketch of the principle behind phased array ultrasound beamforming. The incoming signals are controlled independently, which allows for steering and focusing of the beam.

to be subtracted from the signals, such that further-away signals are shifted forward in time. This ensures that all the waves arrive at the focus point simultaneously and interfere constructively.

2.2 Apodisation

Apodisation is the method of weighting the amplitude of the signal emitted from each transducer element according to a window function. The goal of the apodisation is normally to reduce the prominence of unwanted sidelobes [8]. Signal reflected by the sidelobes can be difficult to differentiate from the reflection of the main beam, such that off-axis reflectors can be misinterpreted as on-axis reflectors. To achieve a reduction of the sidelobes, both sides of the transducer must taper toward zero. The effect that the apodisation has on the beam profile can be understood through the Fourier transform. The shape and width of the beam at the focus point is determined by the Fourier transform of the aperture function, which is altered by the apodisation function. Typically, as sidelobes are suppressed, the main lobe broadens [9].

Some commonly used apodisation functions are the Hamming window, Hann window, Blackman window, and the cosine window [10, 11], all shown in Figure 3. The Fourier transform of these functions are shown in Figure 4, where the different effect they have on the beamforming can be seen. For example, the Blackman window suppresses the sidelobes more aggressively than the Hamming window, but the main lobe is consequently wider.

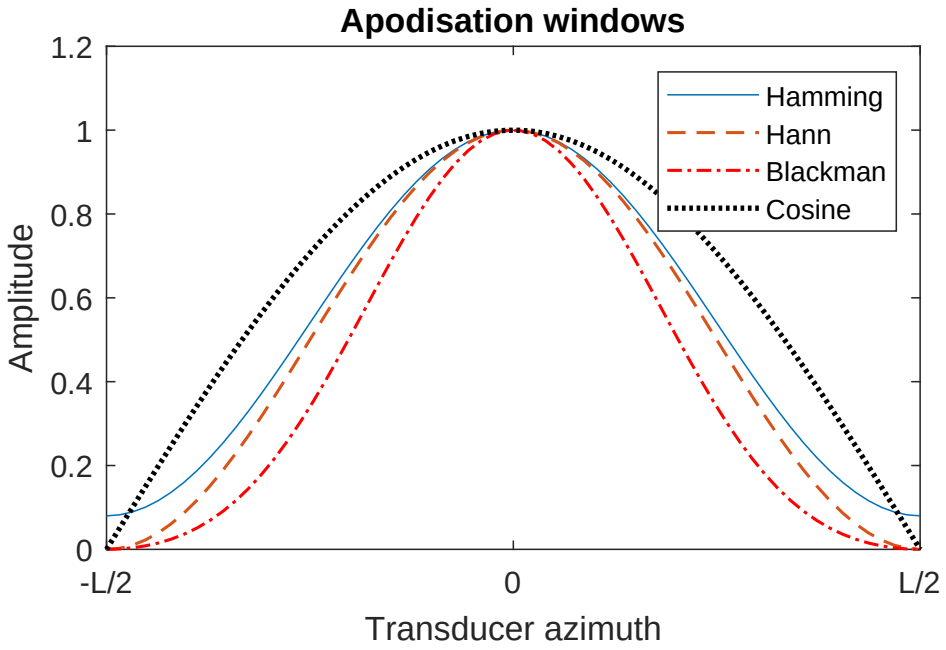

Figure 3: A comparison of apodisation windows along the azimuth of the transducer. The amplitude is tapered off towards the edges of the transducer array.

2.3 Coherence factor

The coherence factor is a commonly used measure of ultrasound beamforming [12]. It gives a measurement between the values 0 and 1, and can therefore serve as a quick quantitative measure of the quality of the beam focus. It is given by

$$CF = \frac{\left|\sum_{i=0}^{N-1} S_i(k)\right|^2}{N \sum_{i=0}^{N-1} |S_i(k)|^2}, \tag{2}$$

for a set of N signals $S_i(k)$ [13]. The numerator measures the coherent energy in the signal, and the denominator the total incoherent energy. This ratio directly relates to the quality of the beam focus; a good focus will have a high proportion of coherent energy, resulting in a higher CF.

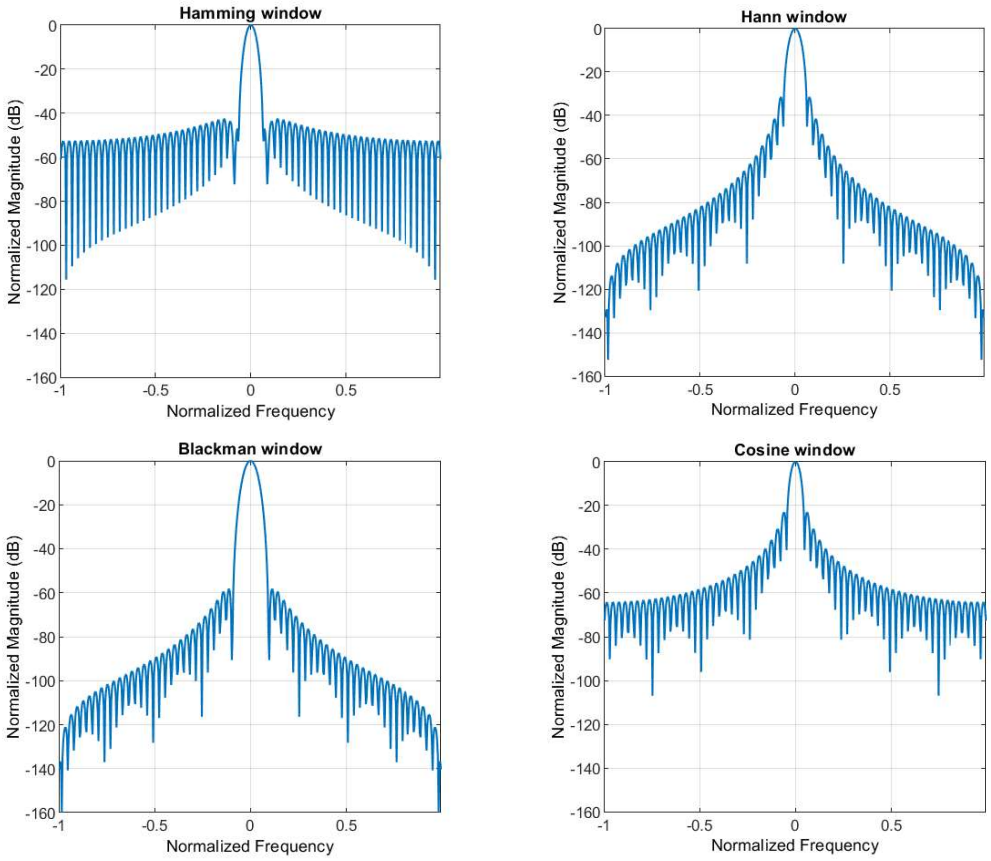

Figure 4: A comparison of the Fourier transform for the different apodisation functions discussed.

2.4 Stress waves in fluid and solid media

Stress waves are mechanical disturbances around the equilibrium state of a material [14]. These disturbances obey a generalized form of Hooke's law (at low enough amplitudes), and will propagate through the material as a wave. Two main types of such waves exist; pressure waves and shear waves. Pressure waves are longitudinal, and stretch and compress the material in the direction of propagation. Shear waves are transversal, such that the layers in the material move from side to side in the direction of propagation.

The propagation speeds of stress waves are governed by the stiffness of the material, which can vary in different directions. The bulk modulus, K, relates

the compression of the material to the stress. The speed of a pressure wave can then be expressed by

$$v_p = \sqrt{\frac{K + \frac{4}{3}G}{\rho}}, \tag{3}$$

where G is the shear modulus, and ρ is the density of the material [14]. Similarly, the speed of a shear wave is

$$v_s = \sqrt{\frac{G}{\rho}}. \tag{4}$$

For all common materials K is positive, such that $v_p > v_s$. Fluid media have a shear modulus of 0, and therefore do not support shear waves [15].

Consider a boundary region between water and steel. An incident pressure wave in the water will be refracted through the steel. This behaviour can be complex, but in short, both pressure waves and shear waves will be induced and propagate through the steel [16]. The angles of refraction for these waves will differ as $v_p > v_s$. Using Snell's law, the critical angles can be calculated as

$$\begin{aligned} \theta_{c,p} &= \arcsin\left(\frac{v_{p,\,steel}}{v_{p,\,water}}\right) \\ \theta_{c,s} &= \arcsin\left(\frac{v_{s,\,steel}}{v_{p,\,water}}\right). \end{aligned} \tag{5}$$

Taking the values $v_{p,\,water} = 1500\,\mathrm{m/s}$, $v_{p,\,steel} = 5780\,\mathrm{m/s}$ and $v_{s,\,steel} = 3130\,\mathrm{m/s}$, the critical angles are $\theta_{c,p} = 15.03°$ for pressure waves and $\theta_{c,s} = 28.63°$ for shear waves. If the incident angle is between these two critical angles, only shear waves will be transmitted into the steel region. This is illustrated in Figure 5, which shows the situation for an incident beam at the critical angle of pressure waves in the steel. The generated pressure waves do not propagate into the steel.

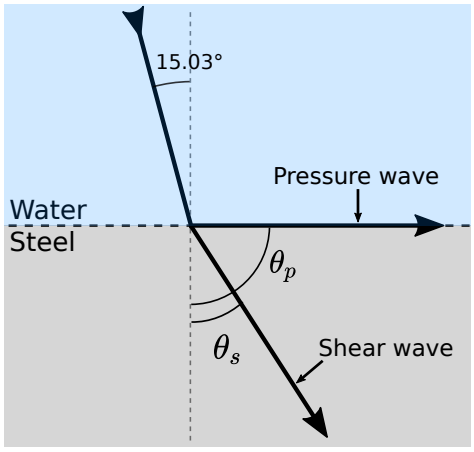

Figure 5: An incident beam of 15.03° induces both pressure waves and shear waves in the steel, but only the shear waves propagate into the body of the steel.

2.5 Simulated annealing

Simulated annealing is an optimisation algorithm originally proposed by Kirkpatrick *et al.* [17]. It is a stochastic method that mimics the effect of annealing in metallurgy, which is the effect where heating up and cooling a metal slowly increases the size of crystals and reduce defects in the structure. In short, the method defines a metaheuristic to search for the global minimum of an objective function in a large search space.

Simulated annealing builds on the Metropolis algorithm, where new states are generated randomly from a Gaussian probability distribution to explore the solution space. In order to minimize an objective function in the solution space, the state exploration needs to be guided somehow. Simulated annealing does this by introducing the concept of a temperature, and this temperature determines if the system accepts and evolves into a new randomly perturbed state. New states that reduce the objective function are always accepted, but states that increase it can also be accepted with a temperature dependent probability. This constitutes a 'thermal fluctuation' in the system, and serves to let the system escape an eventual local minimum.

Early on, the temperature is high and all new states are accepted, regardless of the change in the objective function. The state space is to a large degree roamed freely. As the system cools, inferior states are less and less likely to

be accepted, until no more thermal fluctuations occur. The algorithm will then only accept new states that improve the objective function, and will therefore settle into the nearest local minimum. The intent of the method is that this local minimum is also the global minimum.

The general algorithm can be more formally stated as:

Simulated annealing

1: Initialize to state x_k
2: Calculate initial $E(x_k)$
3: Generate random new state x_{k+1}
4: **if** $E(x_{k+1}) \leq E(x_k)$ **then**
5: Accept state x_{k+1}
6: **else**
7: Accept state x_{k+1} with probability $\exp\{-\frac{\Delta E}{T}\}$
8: **end if**
9: Reduce temperature T, and repeat from step 3
10: Stop when the system is frozen at $T = 0$

2.5.1 Cooling schedule

The cooling schedule that the temperature follows throughout the optimisation algorithm can be set in many different ways, and has a large effect on performance. A slow cooling schedule may help improve exploration of the solution space and convergence toward the global minimum, but it may also increase the computational cost and running time beyond what is practical.

The most simple scheme is to decrease the temperature linearly from the the starting temperature T_0 with a fixed step, such that

$$T_{k+1} = T_k - \Delta T. \tag{6}$$

T_{k+1} is the next temperature step, and T_k is the old value.

A geometrical scheme, proposed by van Laarhoven and Aarts [18], takes the form

$$T_{k+1} = \alpha T_k. \tag{7}$$

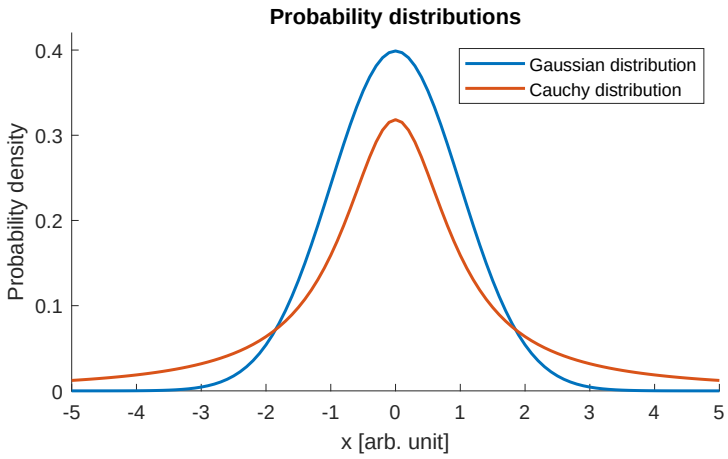

Figure 6: A comparison of the Cauchy and Gaussian probability distributions. The Cauchy distribution is notably more spread out with wider tails.

where α is chosen from the interval $[0.8, 0.99]$. This scheme spends less time at high temperatures, and thus reaches a steady state earlier than the linear scheme. Strenski and Kirkpatrick [19] found no significant difference in performance between the linear and geometric schemes.

An example of a slowly converging scheme is the inverse logarithmic scheme, defined by

$$T_k = \frac{\alpha T_0}{\ln(1+k)}. \tag{8}$$

This schedule decreases more slowly, but improves convergence towards the global minimum [20]. However, the slow speed makes it impractical and computationally expensive.

2.5.2 Fast simulated annealing

The conventional simulated annealing method (CSA) must converge relatively slowly in order to insure proper convergence and avoidance of local minima. An improved method proposed by Szu and Hartley [21], named fast simulated annealing (FSA), seeks to improve the convergence rate while still maintaining good exploration and convergence in the search space. The method uses a Cauchy probability distribution to generate the perturbed states, instead of a Gaussian distribution normally employed by the CSA

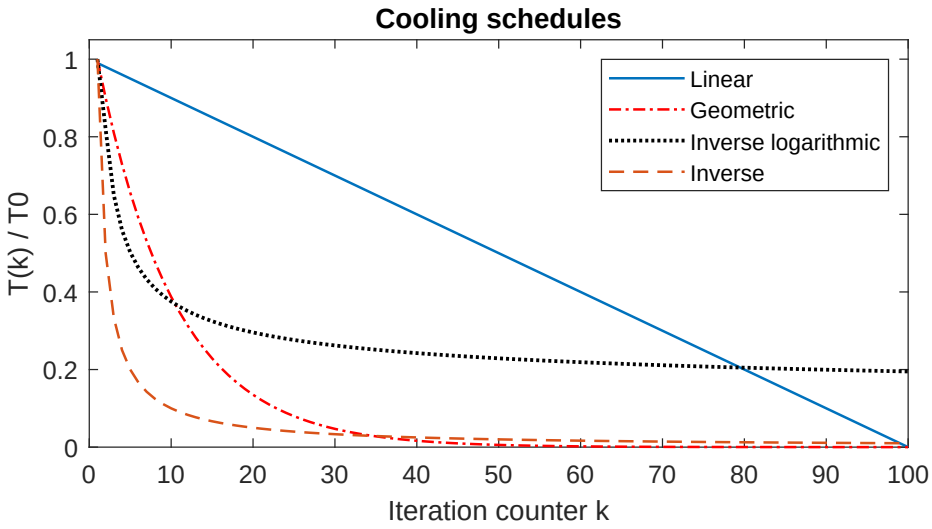

Figure 7: Cooling schedules for the simulated annealing method, shown for up to 100 iterations ($\alpha = 0.9$).

method. These two distributions are shown in Figure 6, where the Cauchy distribution shows notably wider tails than the Gaussian distribution. This leads to occasional long jumps in the solution space, which improves both the exploratory ability of the method, and the ability to escape from local minima. Szu and Hartley show that this allows for the use of a faster cooling schedule that is inversely linear in time:

$$T_k = \frac{T_0}{k}. \tag{9}$$

This significantly improves the convergence rate and running time of the method.

A comparison of all previously discussed cooling schedules are shown in Figure 7. The inverse schedule spends little time at high temperatures, and drops to a value of $T(k)/T_0 = 0.1$ after only 10 iterations. Comparatively, the inverse logarithmic schedule reaches this value after 8100 iterations.

2.5.3 Multivariate Cauchy distribution

Further improvements upon the FSA method are achieved by Lee [22] when investigating multi-dimensional optimisation problems. For such problems,

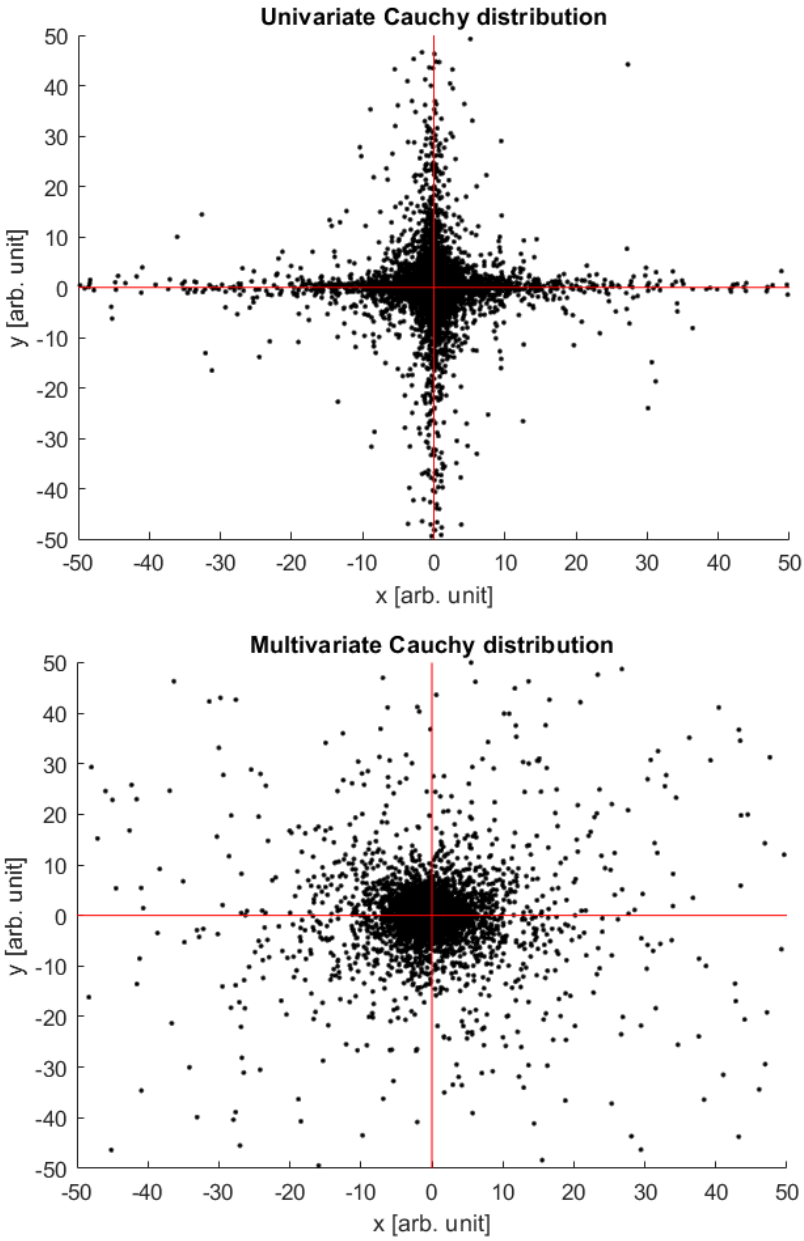

Figure 8: 10 000 random two-dimensional variables, sampled from *(upper)* univariate Cauchy distribution and *(lower)* multivariate Cauchy distribution.

simulated annealing methods conventionally generate individually drawn random variables from univariate probability distributions. Lee proposes a method based on drawing a vector of random variables from a multivari-

ate Cauchy distribution. This is shown to provide better search capability while still allowing for the same cooling schedule as used in one-dimensional problems. Figure 8 shows a comparison of points sampled from the univariate and multivariate distributions. Whereas the points from the univariate distribution appear strongly clustered around the coordinate axes, the points from the multivariate distribution generated by Lee's method show angular isotropy.

3 Method

3.1 General overview

This work seeks to compare methods for determining suitable focusing delays and apodisation functions for use in ultrasound beamforming through a solid plate, in addition to determining where the best focus can be achieved. By testing the quality of the focus at different depths and azimuth values, the benefit of eliminating pressure waves in the steel plate, and thus using a shear-wave based focus, can be investigated.

The proposed method takes advantage of the principle of superposition for waves, in order to significantly speed up testing of different delays. If the amplitudes in the system are low enough that no non-linear behaviour is observed, the principle of additivity ($F(u_1 + u_2) = F(u_1) + F(u_2)$) holds true. For a set of sources u_i, simulating each source separately and adding the acoustic fields from each source together afterwards, will yield the same physical result as simulating all sources being active simultaneously.

After the wave fields from all sources u_i are collected, they can be combined in many different ways; they can all be independently scaled in amplitude and shifted in time. Testing and checking particular configurations of delays and amplitudes can then be done rapidly, and much less computationally expensively compared to running an entirely new simulation with the desired configuration. Although not explored in this project, the size and pitch of the transducer can also be varied. Different methods are then used in order to determine suitable configurations of delays and apodisation functions. In

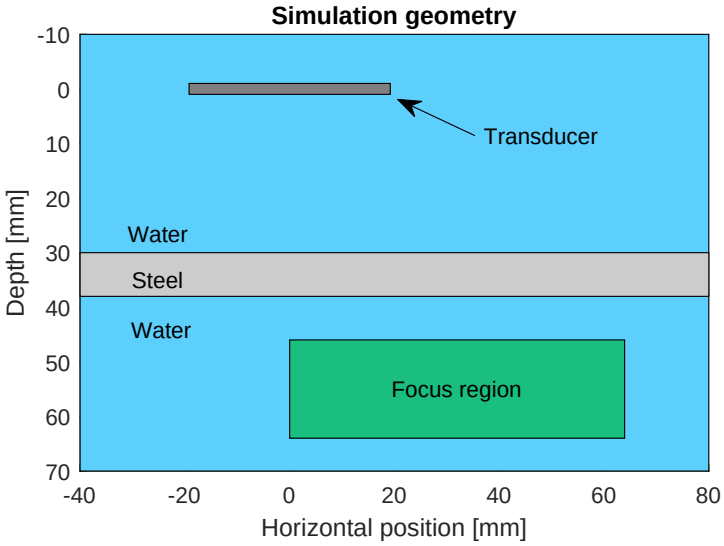

Figure 9: The complete simulation geometry. The focusing methods will be tested and compared in the marked focus region.

summary, the procedure is separated into two stages: one simulation stage and one post-processing stage.

3.2 Simulation stage

Simulation of the ultrasound transducer is done with the finite-difference time-domain software SimSonic [23]. This software solves elastodynamic equations, and can model linear propagation of waves through user-defined media. A transducer is simulated by forcing the field values at a specified location to be equal to the signal waveform.

The simulation geometry is similar to the setup used by Talberg *et al.* [6], and is shown in Figure 9. The inherent translational symmetry in the horizontal direction allows for a significant shortcut to be taken in the simulation stage. If the geometry is extended to infinity in both directions along the x-axis, the wave field from any single transducer element looks identical; it is only translated along the x-axis. Therefore, it is sufficient to simulate only one element of the transducer. The resulting wave from this element can the be shifted horizontally by the desired pitch, and then be superimposed onto itself. This is repeated for however many elements make up the full trans-

Table 1: Material properties set in the SimSonic software.

Material	Property	Value	Unit
Water	ρ	1000	$\mathrm{kg/m^3}$
	v_p	1500	m/s
	v_s	0	m/s
Steel	ρ	8000	$\mathrm{kg/m^3}$
	v_p	5780	m/s
	v_s	3130	m/s

ducer. Furthermore, the wave field can also be shifted through time before the combination step. This allows individual delays to be set for each of the fictional elements. The end result is a full size transducer constructed from the simulation of only one single transducer element, completely controllable through post-processing of the simulation data. This ultimately provides a method for rapid prototyping of transducer parameters, which makes it possible to run optimisation algorithms on these parameters.

The geometrical setup is a 120 mm x 80 mm region, shown in Figure 9. The region consists of water with a steel plate of thickness 8 mm placed in the center, with parameters summarised in Table 1. The region is discretized by 4000x2667 elements of size 0.03 mm. A single transducer element of width 0.51 mm is placed 30 mm above the steel plate, and 20 mm from the left edge. This element will be combined with itself using the aforementioned technique to construct a 64-element transducer with a pitch of 0.6 mm. The element outputs a Gaussian pulse with center frequency of $f_0 = 1.5$ MHz. This system is simulated for 60 μs. Setting the maximum velocity in the solver to 6500 m/s, and the Courant number to 0.9, results in a necessary time step of $dt = 2.9$ ns. The wave field at each time step is stored as a separate snapshot.

3.3 Post-processing stage

After the wave front from the single transducer element is simulated and stored, it can be manipulated in a post-processing stage by superimposing it onto itself. A test of this principle is shown in Figure 10, where the resulting

wave from a 64 element transducer is constructed in two different ways; one by simulating all elements simultaneously in SimSonic, and one by constructing the total wave in the post-processing stage from only 1 transducer element. The reference for the dB scale is the amplitude of the combined wave field directly below the plate, shortly after it is emitted with no focusing applied. Close to the the same wave front is observed in the two cases, with a peak error of -105.8 dB, and mean error of -206.2 dB.

The next part of this stage consists of varying the delays and testing different apodisation functions, in order to find the optimal combination of the

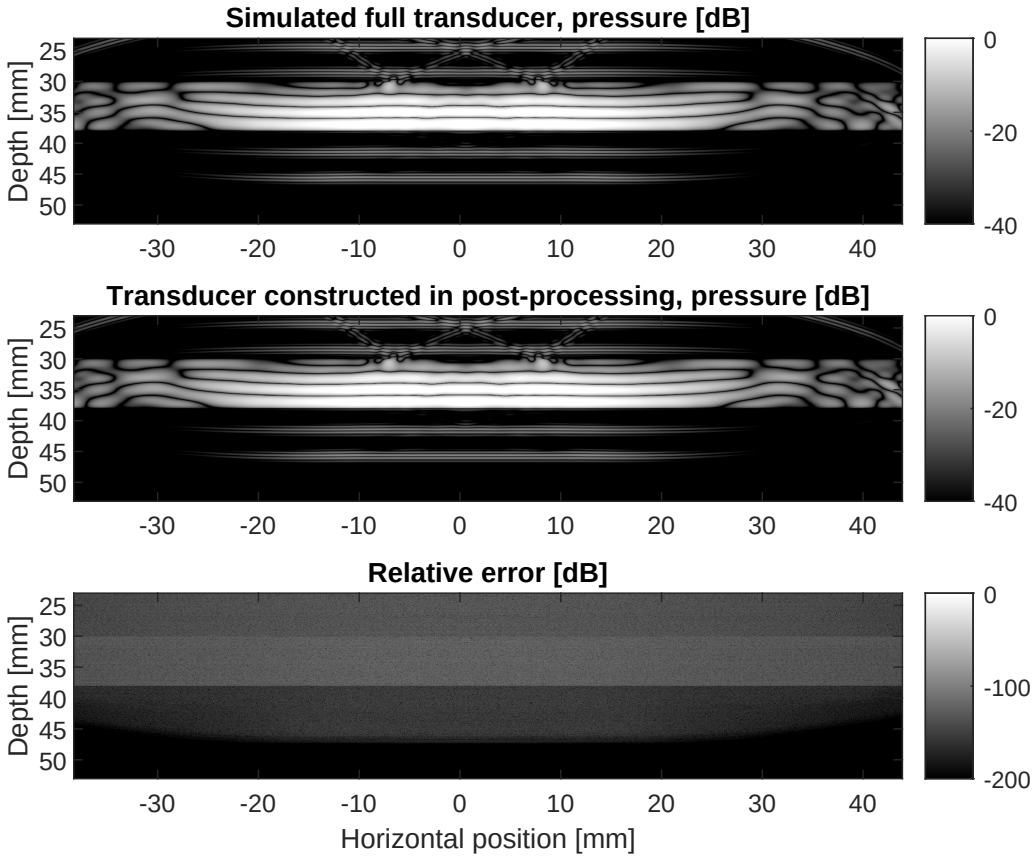

Figure 10: The resulting wave in and below the steel plate, with no focusing. Constructed from 64 transducer elements, (above) with all 64 elements simulated in SimSonic, and (middle) with the wave of 1 element combined with itself 64 times. The two methods produce roughly the same wave field, with a peak error of -105.8 dB, and mean error of -206.2 dB shown in the lower subplot.

simulated wave fronts, through the use of the different methods defined in the following sections. Repeating this for different depths and horizontal locations will give an indication about what regions have the potential for achieving the best focus.

3.3.1 Focusing with Snell's law

The most straight-forward way of focusing is to calculate the travel time of the signal to the focal point. In a homogeneous medium, the delays are calculated from the speed of sound and the distance to the focal point, through the relation seen earlier,

$$\Delta t_i = \frac{r_i}{c}.$$

This gives a largely out of focus pulse due to the refraction of the waves happening in the steel plate.

To achieve a better focus, the steel plate needs to be taken into account. This can be done through careful use of Snell's law,

$$\frac{\sin\theta_1}{v_1} = \frac{\sin\theta_2}{v_2}. \tag{10}$$

θ_1 and θ_2 are the incident and transmitted angles of an incoming beam crossing into a new medium, where v_1 and v_2 denote the speed of sound in these two mediums.

Figure 11 depicts a situation where a ray travels from point P to Q, and passes through a medium with a slower speed of sound. For a given set of points P and Q, the vertical distances Δy_1, Δy_2, Δy_3, and the total length l will always be known, but the individual horizontal distances Δx_1, Δx_2, and Δx_3 will depend on the angle of refraction. With the variables denoted in the figure, we can set up an equation relating the horizontal distances to the angles θ_1 and θ_2:

$$\begin{aligned} l &= \Delta x_1 + \Delta x_2 + \Delta x_3 \\ &= (\Delta y_1 + \Delta y_3)\tan\theta_1 + \Delta y_2 \tan\theta_2. \end{aligned} \tag{11}$$

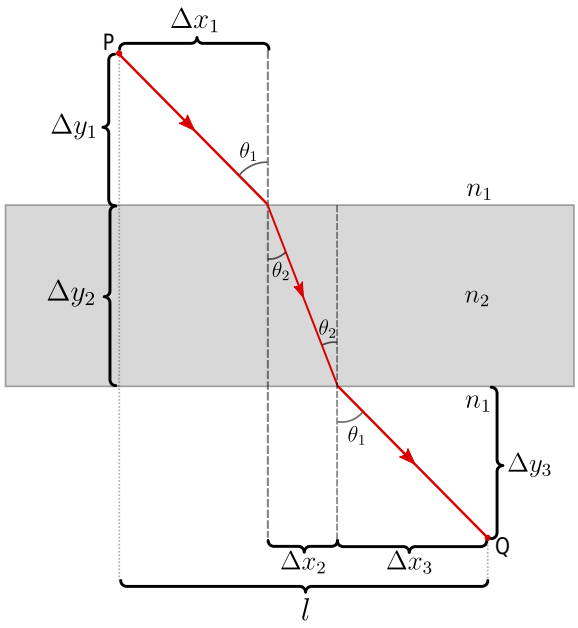

Figure 11: Refraction of single a ray through a solid plate, travelling from point P to point Q.

Using Snell's law (10) to express θ_2 in terms of θ_1, we get

$$l = (\Delta y_1 + \Delta y_3)\tan\theta_1 + \Delta y_2 \tan\left(\arcsin\left(\frac{v_2}{v_1}\sin\theta_1\right)\right) \tag{12}$$

This equation can be difficult to solve analytically for the incident angle θ_1, but it can easily be solved numerically instead.

The total time taken for a beam to travel from point P to point Q can finally be calculated as

$$\begin{aligned}\Delta t &= \frac{\sqrt{\Delta y_1^2 + \Delta x_1^2}}{v_1} + \frac{\sqrt{\Delta y_2^2 + \Delta x_2^2}}{v_2} + \frac{\sqrt{\Delta y_3^2 + \Delta x_3^2}}{v_1} \\ &= (\Delta y_1 + \Delta y_3)\frac{\sqrt{1+\tan^2\theta_1}}{v_1} + \frac{\sqrt{(l - \Delta y_1 \tan\theta_1)^2 + \Delta y_2^2}}{v_2}\end{aligned} \tag{13}$$

As described in section 2.4, the solid plate can support both shear waves and pressure waves, which travel at different speeds in the material. One must therefore choose to use either shear waves or pressure waves in the plate when calculating focus delays through Snell's law. Note that above

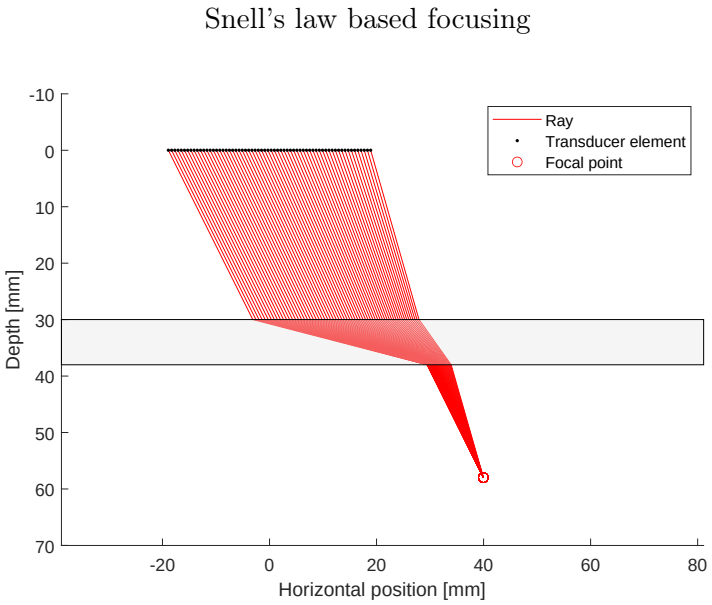

Figure 12: An example of focusing with Snell's law, showing the path of the rays from each individual transducer element to the focus point. Shear waves in the steel plate are used.

the critical angle of $\theta_{c,p} = 15.03°$ for pressure waves, only shear wave based focusing is possible.

Thus, by solving equations (12) and (13) sequentially for each element on the transducer, the steel plate can be taken into account when calculating focus delays. An example of how this looks is shown in Figure 12. Rays from each transducer element are shown to refract through the steel plate, meeting up at the desired focus point.

3.3.2 Focusing with amplitude peak alignment

When performing the linear combination of the single transducer element to construct the full transducer, the signal from each fictional element is stored and available separately. It can be seen from these signals approximately when the signal pulse arrives at the focus point. A simple method of focusing then consists of aligning each of these signals, such that highest peaks of the signals overlap. This results in the largest possible amplitude for the combined pulse, but may or may not provide good focusing in terms of full-width

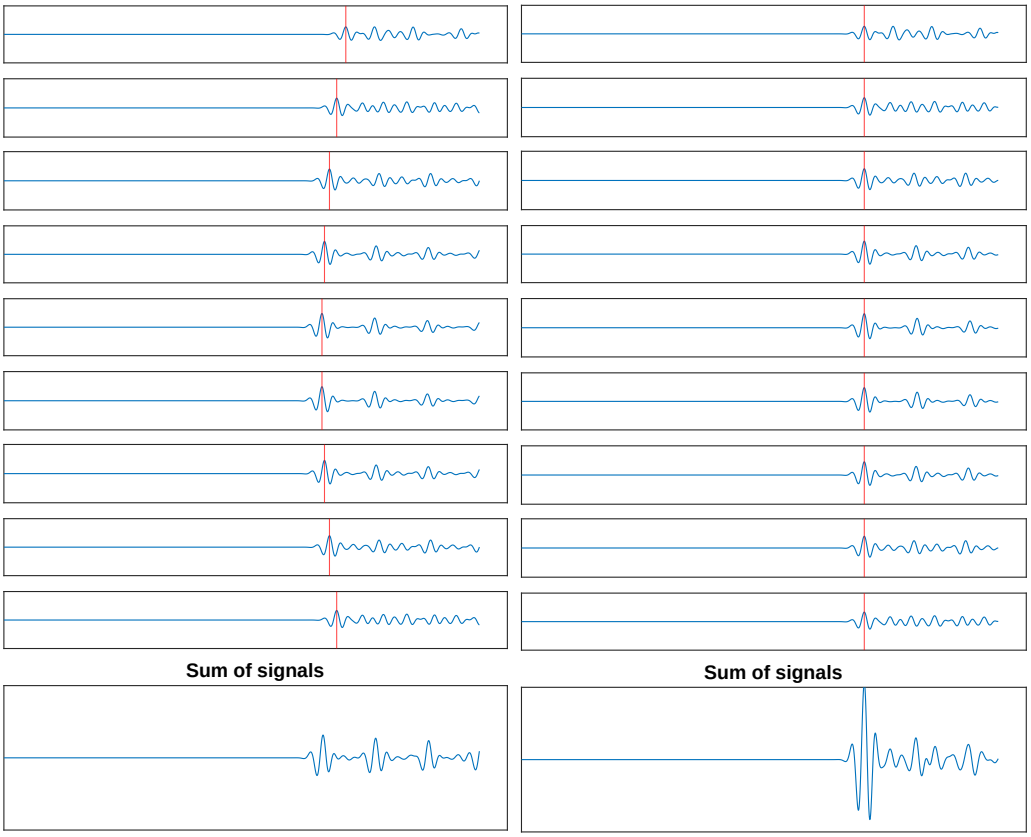

Figure 13: Focusing done using amplitude alignment. The vertical red lines indicate the location of the highest peak. When focusing, the signals are shifted such that these peaks overlap, yielding the highest amplitude possible at the focus point. This also demonstrates the basic idea of ultrasound focusing.

half-maximum value or noise. This method is illustrated in Figure 13, where focusing is attempted through the steel plate directly below the transducer. The signal from the centermost elements arrives at the focus point first, so these have to be delayed such that they all arrive simultaneously.

In a homogeneous medium, this method simply gives the standard analytical solution for the focusing delays. It effectively measures the travel time of the wave from each transducer element to the focus point, instead of calculating it from the distance and speed of sound in the medium. When focusing through a solid plate, it is not so clear if this method provides the best focus, because of the noise introduced by internal reflections and ringing in the

plate.

This method has an additional interesting effect when used to focus through a steel plate. When focusing directly below the transducer, waves transmitted by pressure waves in the steel plate arrive first and have the highest amplitude. Above the critical angle, waves transmitted by shear waves in the plate have the highest amplitude. In the transition region around the critical angle, some signals will have the highest amplitude for the pressure-wave transmitted pulse, and some signals will have the highest amplitude for the shear-wave transmitted pulse. When aligning these signals at their highest amplitudes, a combination of pressure and shear waves in the steel plate is used to form the focused pulse. This effect is investigated to see if it leads to an improvement in focus quality and reduced noise.

3.3.3 Focusing with simulated annealing

For this project, the fast simulated annealing method described in section 2.5.2 is used. The states x describe different sets of focus delays, where $E(x)$ is a score function that evaluates the quality of the focus for a state x. The solution space then consists of all possible combinations of focus delays.

Two variations of the procedure are compared in order to determine which one is most suitable. In the first variation, the new state x_{k+1} are sampled from the multivariate Cauchy distribution. The second variation samples from the Gaussian distribution. This, as discussed, affects the locality of the search. The new states are evaluated by the score function, and then accepted or rejected with a temperature dependent probability. This makes up one iteration of the procedure. Iterations continue until the system appears frozen, i.e. when no new states have been accepted in the last 100 iterations.

The temperature is gradually lowered throughout the procedure with the inverse cooling schedule

$$T(k) = \frac{T_0}{k}, \tag{14}$$

where k is the iteration counter.

The optimisation algorithm requires a set of initial delays x_1 to start iterating from. A good initial guess is important to ensure good results. A naive initial guess can be made by ignoring the steel plate, and assuming instead that the region is homogeneous and consisting entirely of water. A better initial guess can be calculated from Snell's law based focusing, with the steel plate taken into account. A semi-local search is done from this starting point, with the hope of determining a more suitable set of focus delays. When the focus point lies below the critical angle, p-wave based focusing is used. When the focus point lies above the critical angle, s-wave based focusing is used. Similarly to the amplitude alignment method, this method can take advantage of the combination of shear waves and pressure waves in the steel plate in the transitional region around the critical angle.

The score function $E(x)$ considers three different metrics at the focus point: the coherence factor, the peak amplitude, and a time integral ratio of the signal. This ratio is the ratio between the integral of the squared main pulse, divided by the integral of the squared signal leading and trailing the main pulse. These values are normalized to the range $[0, 1]$ and weighted equally in a sum.

A major challenge for the simulated annealing method is the high dimensionality of the problem. A transducer consisting of 64 elements naturally leads to a problem of dimensionality 64, as the delays for the elements can all be adjusted separately. A problem of such high dimensionality has a very large solution space, which is difficult to search efficiently.

Making assumptions about the delay curve can help mitigate some of the complexity by reducing the high dimensionality. Mainly, it is assumed that two neighbouring transducer elements will have a similar delay. In other words, the delay curve will have no overly sharp jumps.

With this assumption in mind, an interpolation method for determining delays can be used. An evenly spaced subset of the full set of delays is considered, and the full set is found by interpolating between the delays in this subset. An example of this method is shown in Figure 14. Interpolation is done by the method of splines with the modified Akima method [24]. A

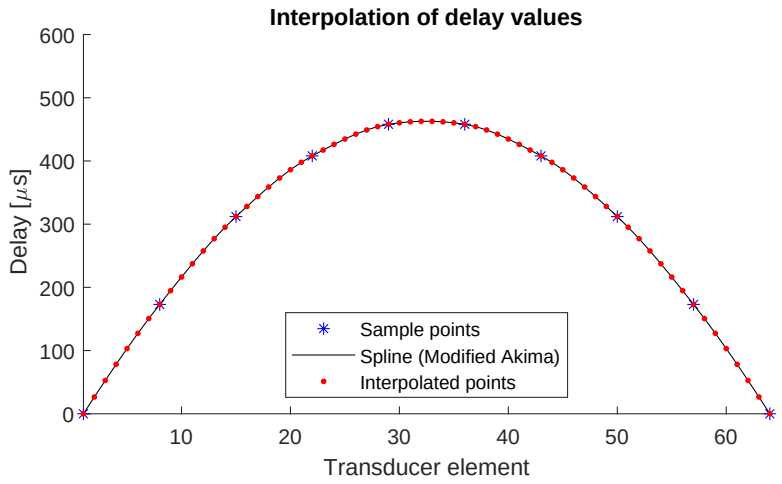

Figure 14: Delay curve calculated from interpolating between a subset of delays, for a sample focusing situation.

spline is fitted for the selected subset of delays, and the rest of the delays are sampled from the interpolating spline.

To check that the simulated annealing method gives reasonable results, it can be checked against a known analytical solution. If the region is simplified to contain only water, the analytical solution is given by the distance and speed of sound in water ($\Delta t_i = \frac{r_i}{c}$, subtracted from the signals). The method can then be tested by starting off with a bad solution, and seeing if the analytical solution is reached by the optimisation method. Figure 15 shows the result of such a test, where the solver was given a largely out of focus initial guess, but succeeded in finding a good approximation to the correct solution.

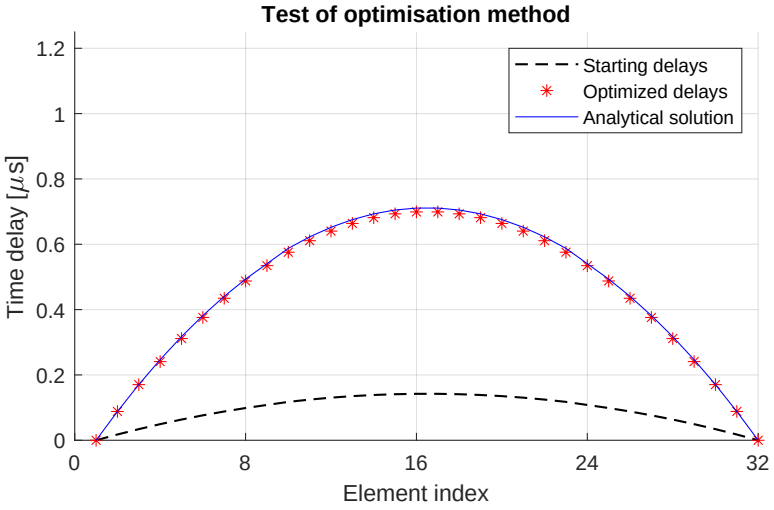

Figure 15: Test of optimisation algorithm, showing that a close approximation to the analytical solution was found from a bad initial guess.

4 Results

4.1 Comparison of apodisation functions with Snell's law based focusing

Table 2 shows the mean value of the different evaluation metrics for the different apodisation windows, for Snell's law shear-wave based focusing. All dB values are in reference to the amplitude of the wave field directly below the plate, shortly after it is emitted with no focusing applied. Depth and horizontal distances follow the same coordinate system as used in section 3.1 in Figure 9, in which the origin of both axes are set to the center of the transducer. The uniform window resulted in the lowest FWHM, showing the effect of main beam broadening when using an apodisation window. The highest time-integral value was achieved with the Hamming window. The effect of apodisation can be seen more clearly in Figures 16, where the spatial pulse at the focus point is shown for the uniform window and the Hamming window. Only the focus region below the plate is shown. The pulse is focused at a horizontal position of $x = 40$ mm and a depth of $y = 56$ mm. The effect of all apodisation windows is a less noisy pulse, but a higher FWHM value.

Table 2: Mean values for different apodisation windows used with Snell's law based focusing.

Window	Amplitude [dB]	FWHM [mm]	Time integral [ratio]
Uniform	-12.20	0.62	2.25
Hamming	-11.01	0.90	2.36
Hann	-10.65	0.91	2.29
Blackman	-10.26	0.94	2.24
Cosine	-11.24	0.89	2.21

4.2 Comparison of focusing methods

Figure 17 shows the distribution of evaluation metrics over the entire focusing region, for the Snell's law based focusing with shear waves, with Hamming apodisation. Data for the alignment method is shown in Figure 18. Each

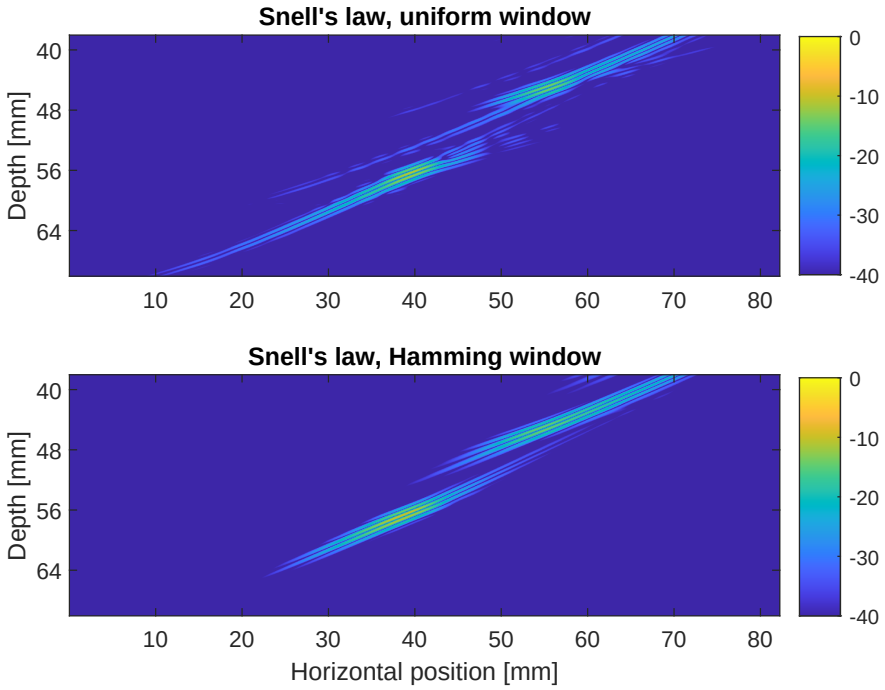

Figure 16: A comparison of the pulses with no apodisation, and apodisation with the Hamming window.

pixel in the plot indicates the value of the given metric when the pulse is focused at that specific point in the region. White pixels indicate missing data, for instance when the location of the FWHM lies outside the simulation region. The mean and peak values of the metrics for all focusing methods are shown in Table 3.

Figure 19 shows the normalised time signal for focusing with Snell's law at $x = 0$ mm with pressure waves, and $x = 40$ mm with shear waves, at

Table 3: Mean and peak (shown in parenthesis) values over the entire region for all focusing methods, all using the Hamming window.

Method	Amplitude [dB]	FWHM [mm]	Time integral [ratio]
Alignment	-7.82 (-6.35)	0.51 (0.27)	2.85 (3.62)
Snell's law (s-wave)	-11.01 (-7.27)	0.90 (0.45)	2.36 (3.80)
Snell's law (p-wave)	-8.26 (-7.43)	0.42 (0.38)	1.51 (2.20)
Sim. ann. Cauchy distr.	-11.54 (-7.24)	0.83 (0.26)	2.94 (4.52)
Sim. ann. Gauss distr.	-11.28 (-7.26)	0.87 (0.37)	3.07 (4.35)

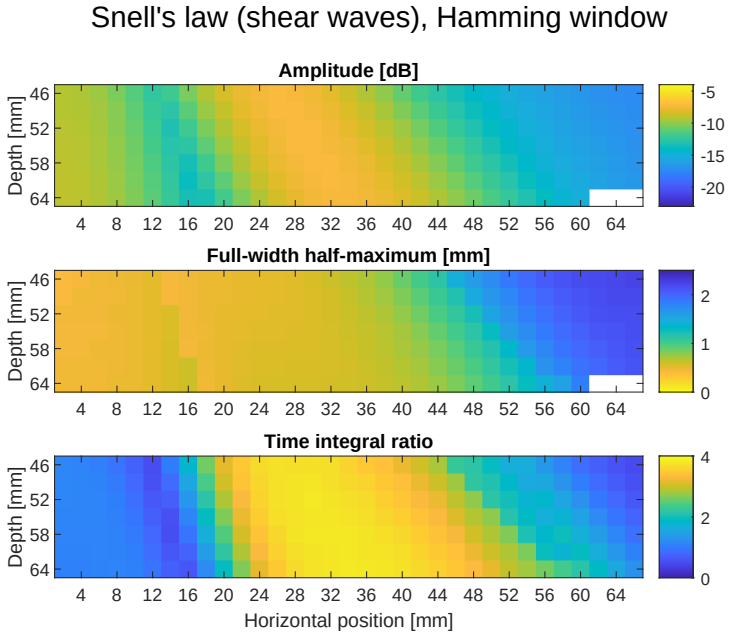

Figure 17: Distribution of the evaluation metrics over the focusing region, using the Snell's law method with shear waves.

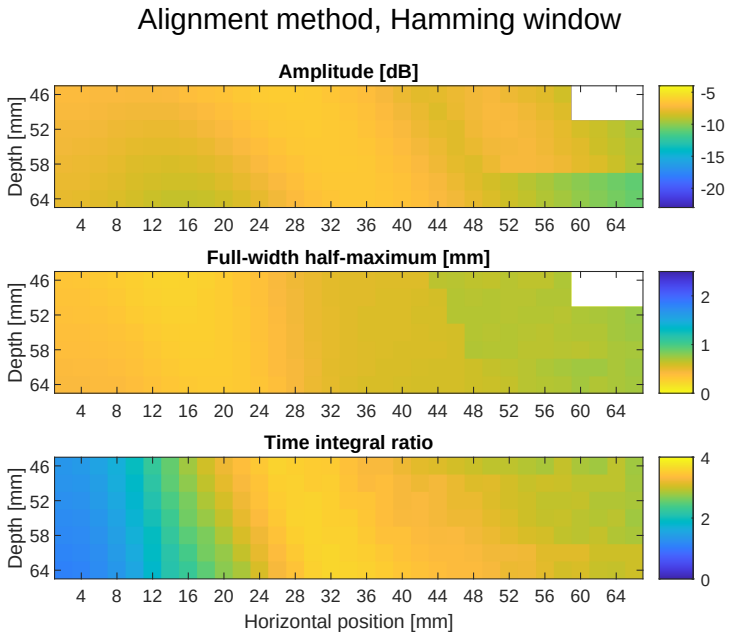

Figure 18: Distribution of the evaluation metrics over the focusing region, using the amplitude alignment focusing method.

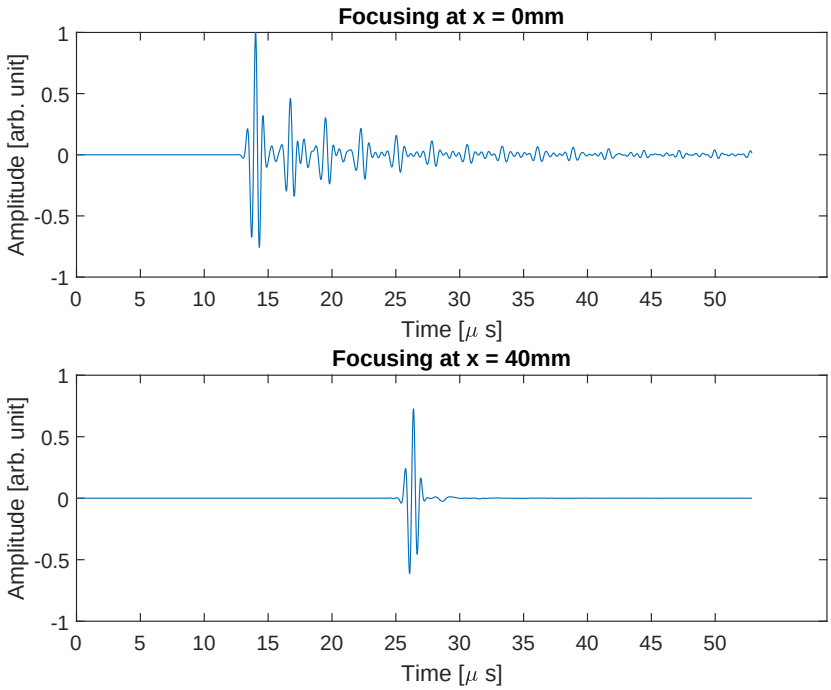

Figure 19: The received signal at the focus point, using focusing with Snell's law at two different horizontal positions, at depth $y = 56$ mm. Note the difference in the amount of ringing trailing behind the main pulse for the two signals.

depth $y = 56$ mm. The difference in noise and ringing in the signal is seen, demonstrating the benefit of operating above the critical angle for pressure waves.

Figure 20 shows the resulting pulse from the amplitude alignment method and the two simulated annealing methods with Cauchy and Gauss distributions. The alignment method appears to have more sidelobes than the simulated annealing methods. The peak amplitude values at the focal point are -7.26 dB, -9.73 dB and -9.70 dB respectively. FWHM values are 0.57 mm, 0.67 mm and 0.67 mm. A sample delay curve for focusing at $x = 40$ mm, with development of the score function throughout the simulated annealing run, is shown in Figure 24. The result from the optimisation is approximately the same as the original delays calculated from Snell's law. For both simulated annealing methods, there is a region between $x \in [16, 20]$ mm where the time integral ratio is higher than the other methods, as can be seen in Figures 21 and 22. A comparison of pulses at $x = 20$ mm, generated from Snell's law focusing and simulated annealing is shown in Figure 23.

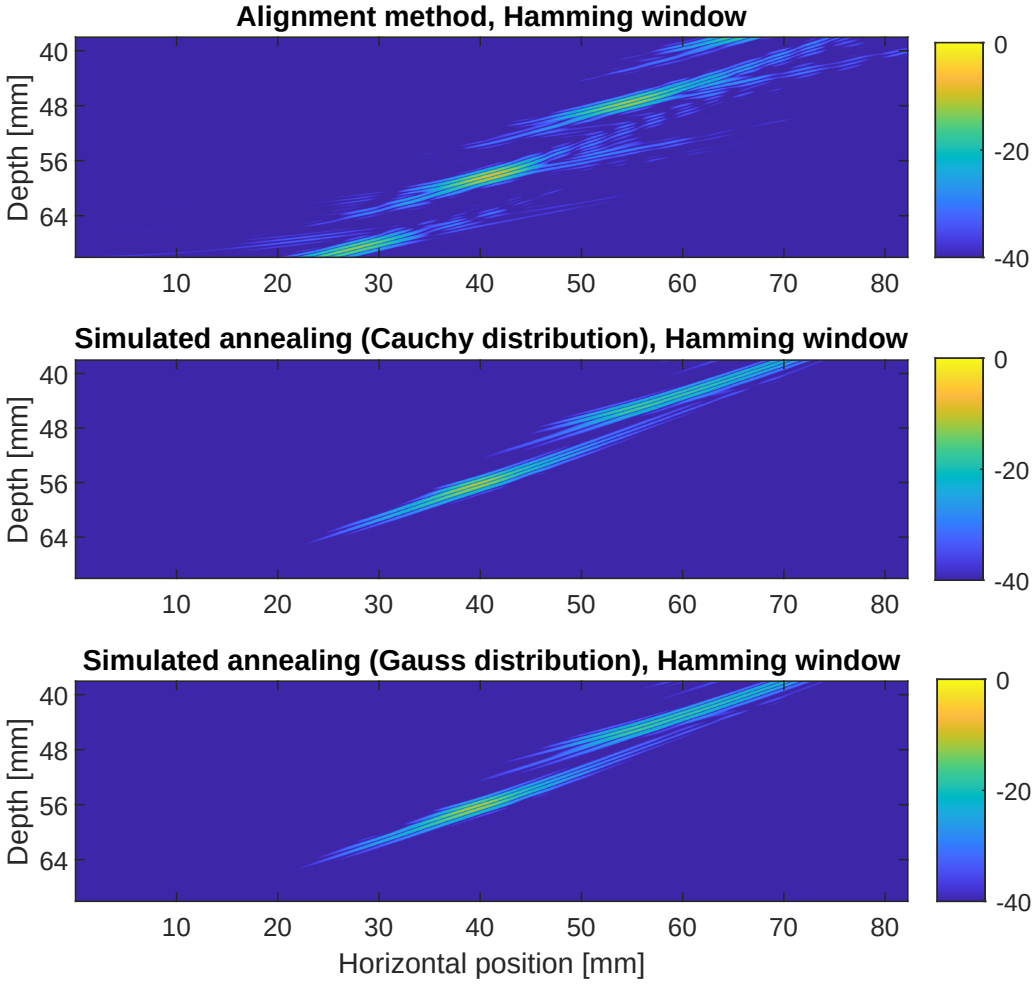

Figure 20: Focusing at $x = 40$ mm and $y = 56$ mm, for the amplitude alignment method and both simulated annealing methods. Amplitude alignment method appears to produce a noisier pulse.

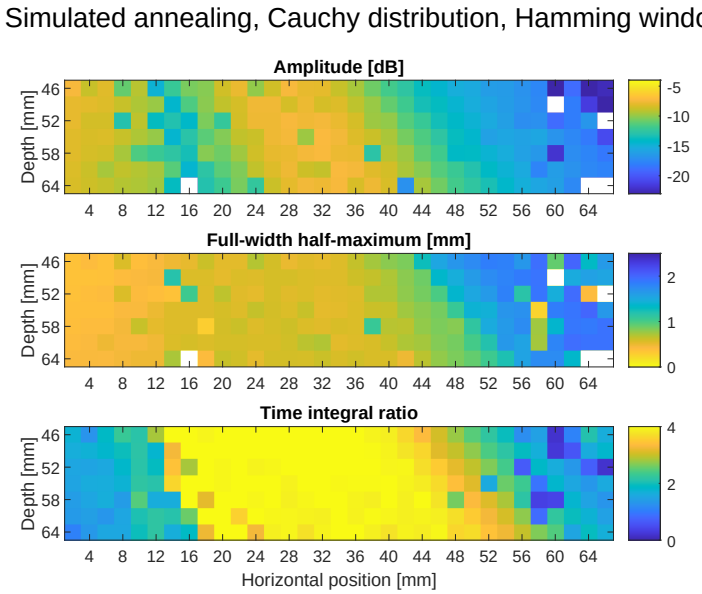

Figure 21: Distribution of the evaluation metrics over the focusing region, using the simulated annealing method with a Cauchy probability distribution.

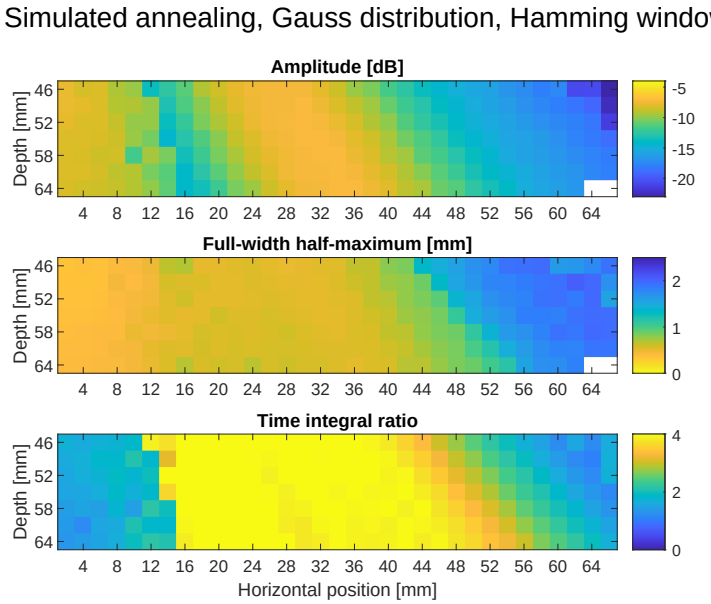

Figure 22: Distribution of the evaluation metrics over the focusing region, using the simulated annealing method with a Gaussian probability distribution.

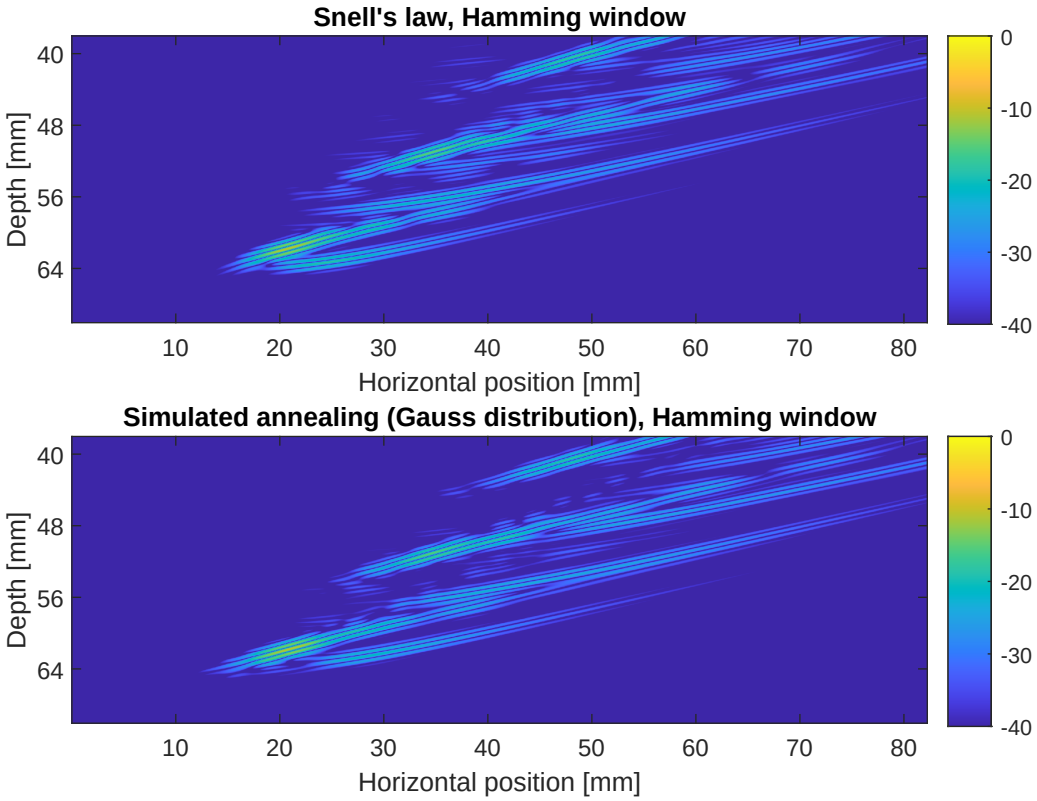

Figure 23: Focusing at $x = 20$ mm and $y = 60$ mm *Upper:* Pulse from Snell's law. *Lower:* Pulse from simulated annealing, performed using the delays from Snell's law as initial delays.

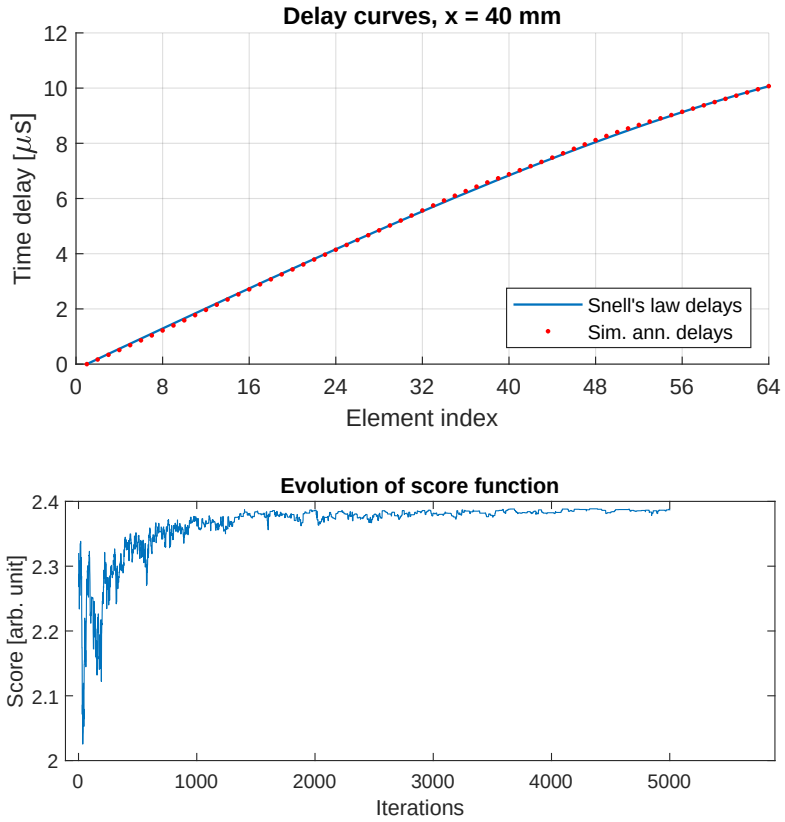

Figure 24: Result of a simulated annealing run, with delays calculated from Snell's law used as initial delays. Approximately the same delays are reconstructed.

5 Discussion

The technique of superposition to construct the full transducer in a post-processing stage allowed for a significant speedup in testing the various methods of focusing. As it was not necessary to run new FDTD simulations for every configuration, testing the quality of focus across the investigated region was possible in a few hours, depending on the method used. The recorded wave field from the single transducer element, collected in the SimSonic simulation, amounted to approximately 800 GB with the resolution of 4000x2667 and time step of 2.9 ns. This dataset would normally have to be re-computed for every configuration of focusing delays. However, the geometry must be translationally symmetric for the method to be applicable.

5.1 Apodisation functions

Using apodisation proved beneficial to the focusing quality of all investigated methods. There was a notable reduction in noise when apodisation was used, but also a broadening of the main lobe, indicated by the increased FWHM values seen in Table 2. This was the case for all apodisation windows, but the Hamming window produced the cleanest signal with the least noise. The Blackman window was the worst performing window in this experiment.

5.2 Location of focusing

There is a clear advantage in focusing above the critical angle of pressure waves in the steel plate. Consider Figure 17 showing the evaluation metrics of Snell's law based focusing. Starting at $x = 0$ mm, the peak amplitudes are relatively high, but the signal suffers from severe ringing. This stems from the reverberations of the stress waves in the steel plate that continuously bounce back and forth. These reverberations take a long time to die out, as the stress waves propagate perpendicularly to the plate surface.

Next, the region $x \in [12, 20]$ mm has poor focusing quality. This results from interaction between the waves transmitted by pressure waves and shear waves in the steel plate. In this region, the two types of waves arrive at the focus point approximately at the same time, and interfere negatively.

In the range $x \in [24, 40]$ mm, focusing quality is the highest. This is the most apparent from the time integral ratio, which shows clear separation between good and bad regions. The peak amplitudes are heightened in this region, and the FWHM still retains a relatively low value. In Figure 19, it can again be seen that the ringing has been almost entirely eliminated at the horizontal position of $x = 40$ mm.

Past the point of $x = 40$ mm, the amplitude of the signal starts to decay, and gets lower and lower with an increasing angle. Furthest to the right, one starts to approach the critical angle of the shear wave in the steel plate. At that point it is no longer possible to transmit any significant amount of energy through the plate, and no useful focusing can be achieved.

5.3 Focusing methods

By looking at Figure 18, the amplitude alignment method at first glance seems to be a good candidate for focusing, as the recorded metrics look as good as, or better than, the Snell's law based focusing metrics discussed above. The peak amplitudes are the highest of all methods at all sampled points, as would be expected from the nature of the method. The FWHM values are among the lowest, with a mean value of 0.51 mm, compared to 0.90 mm for Snell's law based focusing. However, looking at the spatial pulse in Figure 20, the amplitude alignment method causes additional sidelobes, with relatively high peak amplitudes in relation to the main lobe. Reflections from these sidelobes can be more easily misinterpreted as reflections from the main lobe.

Focusing with Snell's law reliably produces good results at a low computational cost. The method works best in the region around $x \in [24, 40]$ mm, where mostly shear waves are transmitted through the plate, and most of the pressure waves in the steel are refracted away. Additionally, the shear wave also bounces up and down inside the steel plate. At higher angles, the shear wave will have travelled further horizontally before it hits the interface with the water below the plate. The effect of this can be seen by comparing Figures 16 and 23. In the first figure, two separate pulses are seen, stemming

from the resonating shear wave in the plate. In the second figure, where focusing is done close to the vertical axis, more ringing is observed, with less spacing between the separate pulses.

The simulated annealing method produced results that were in most cases approximately the same as the initial delays calculated by Snell's law. Where the optimisation was successful, the results were close to identical, as seen in Figure 24. The solution state makes a short detour from the initial state, and quickly recovers the initial solution. It then settles into the local minimum around the initial solution, making only minute adjustments to optimise the metrics that are taken into account by the score function.

The distribution of evaluation metrics with Cauchy simulated annealing (Figure 21 shows some randomness in the values. In these cases, the solution state has wandered far off from the initial state, and struggled to recover good solutions. This is due to the long tails of the Cauchy probability distribution, which routinely makes the solution do much longer jumps than the Gaussian. The Gaussian distribution, as expected, exhibits less of this randomness. If the starting temperature is increased to improve the exploratory property of the optimisation, this randomness was very high with a large chance of the solution becoming stuck in a sub-optimal local minimum. This suggests that the method of simulated annealing is not suited for the given problem, as any improvement to the focusing was found to be very small, while being extremely computationally heavy.

Of special interest was the transitional region between where the pressure waves dominate, and where the shear waves dominate. The methods of amplitude alignment and simulated annealing both had the possibility of combining the pressure waves and shear waves in a beneficial way, but this was mostly detrimental to the quality of the focus, and no significant improvement was achieved in this region.

6 Conclusion

This project has explored the usage of a post-processing method based on the superposition principle of waves for performing rapid experimentation with different beamforming parameters. New configurations can be tested in seconds, without running costly FDTD simulations, which took upwards of 6 hours with the geometry and timescale used in the project.

A range of focusing methods have been tested in a region below the steel plate. Focusing by Snell's law using shear waves in the steel plate was found to provide good focusing capabilities, as originally proposed by Talberg *et al.* [6]. The problem of ringing in the plate was effectively eliminated when focusing in the region $x \in [2440]$ mm at all depths, as the interference from pressure waves in the plate is reduced.

The amplitude alignment method for focusing resulted in a noisier signal with stronger sidelobes in most cases. Algorithmic optimisation of the delays through simulated annealing did not provide reliable improvements over Snell's law based focusing, and is also computationally expensive.

None of the focusing methods tested in this project were able to take advantage of the combination of pressure waves and shear wave in the steel plate, in the transition region around the critical angle of pressure waves.

Future work lies in applying the methods to more complex geometries, and exploring the effect of concrete existing behind the steel plate. When good focusing is been determined in the concrete layer, applying focusing also to the received signal can be done to improve the ability to identify defects in the concrete.

References

[1] E. M. Viggen, I. A. Merciu, L. Løvstakken, and S.-E. Måsøy, "Automatic interpretation of cement evaluation logs from cased boreholes using supervised deep neural networks," vol. 195, p. 107539, 2020.

[2] B. Froelich, A. Dumont, D. Pittman, and B. Seeman, "Cement evaluation tool: A new approach to cement evaluation," vol. 34, no. 8, pp. 1835–1841.

[3] R. M. Havira, "Ultrasonic cement bond evaluation." OnePetro.

[4] A. J. Hayman, R. Hutin, and P. V. Wright, "High-resolution cementation and corrosion imaging by ultrasound." Society of Petrophysicists and Well-Log Analysts, 1991.

[5] R. van Kuijk, S. Zeroug, B. Froelich, M. Allouche, S. Bose, D. Miller, J.-L. Le Calvez, V. Schoepf, and A. Pagnin, "A novel ultrasonic cased-hole imager for enhanced cement evaluation." International Petroleum Technology Conference, 2005.

[6] A. S. Talberg, T. F. Johansen, S.-E. Masoy, T. Rommetveit, S. Brekke, and H. Dong, "Ultrasonic focusing through a steel layer for acoustic imaging," in *2018 IEEE International Ultrasonics Symposium (IUS)*. IEEE, 2018, pp. 1–4.

[7] L. Demi, "Practical guide to ultrasound beam forming: Beam pattern and image reconstruction analysis," vol. 8, no. 9, p. 1544, 2018, number: 9 Publisher: Multidisciplinary Digital Publishing Institute.

[8] T. L. Szabo, "Chapter 6 - beamforming," in *Diagnostic Ultrasound Imaging: Inside Out (Second Edition)*, second edition ed., T. L. Szabo, Ed. Boston: Academic Press, pp. 167–207.

[9] f. harris, "On the use of windows for harmonic analysis with the discrete fourier transform," vol. 66, pp. 51–83.

[10] K. J. Parker, "Correspondence: Apodization and windowing functions," vol. 60, no. 6, pp. 1263–1271. [Online]. Available: https://ieeexplore.ieee.org/document/6521077/

[11] A. Nuttall, "Some windows with very good sidelobe behavior," vol. 29, no. 1, pp. 84–91.

[12] Pai-Chi Li and Meng-Lin Li, "Adaptive imaging using the generalized coherence factor," vol. 50, no. 2, pp. 128–141, 2003, conference Name: IEEE Transactions on Ultrasonics, Ferroelectrics, and Frequency Control.

[13] K. W. Hollman, K. W. Rigby, and M. O'Donnell, "Coherence factor of speckle from a multi-row probe," in *1999 IEEE Ultrasonics Symposium. Proceedings. International Symposium (Cat. No.99CH37027)*, vol. 2, 1999, pp. 1257–1260 vol.2, ISSN: 1051-0117.

[14] P. Myler and L. M. Wyatt, "8 - mechanics of solids," in *Mechanical Engineer's Reference Book (Twelfth Edition)*, E. H. Smith, Ed. Butterworth-Heinemann, 1994, pp. 8–1, num Pages: 8-42.

[15] "Oblique incidence," in *Ultrasonic Guided Waves in Solid Media*, J. L. Rose, Ed. Cambridge University Press, 2014, pp. 67–75.

[16] "Reflection and refraction," in *Ultrasonic Guided Waves in Solid Media*, J. L. Rose, Ed. Cambridge University Press, 2014, pp. 53–66.

[17] S. Kirkpatrick, C. D. Gelatt, and M. P. Vecchi, "Optimization by simulated annealing," vol. 220, no. 4598, pp. 671–680, 1983.

[18] P. J. M. van Laarhoven and E. H. L. Aarts, *Simulated Annealing: Theory and Applications*. Springer Netherlands, 1987.

[19] P. N. Strenski and S. Kirkpatrick, "Analysis of finite length annealing schedules," vol. 6, no. 1, pp. 346–366, 1991.

[20] S. Geman and D. Geman, "Stochastic relaxation, gibbs distributions, and the bayesian restoration of images," vol. PAMI-6, no. 6, pp. 721–741, 1984.

[21] H. Szu and R. Hartley, "Fast simulated annealing," vol. 122, pp. 721–741.

[22] C.-Y. Lee, "Fast simulated annealing with a multivariate cauchy distribution and the configuration's initial temperature," vol. 66, no. 10, pp. 1457–1466. [Online]. Available: https://doi.org/10.3938/jkps.66.1457

[23] E. Bossy, "*SimSonic: FDTD simulation of ultrasound propagation*." [Online]. Available: http://www.simsonic.fr/index.php

[24] H. Akima, "A new method of interpolation and smooth curve fitting based on local procedures," vol. 17, no. 4, pp. 589–602.

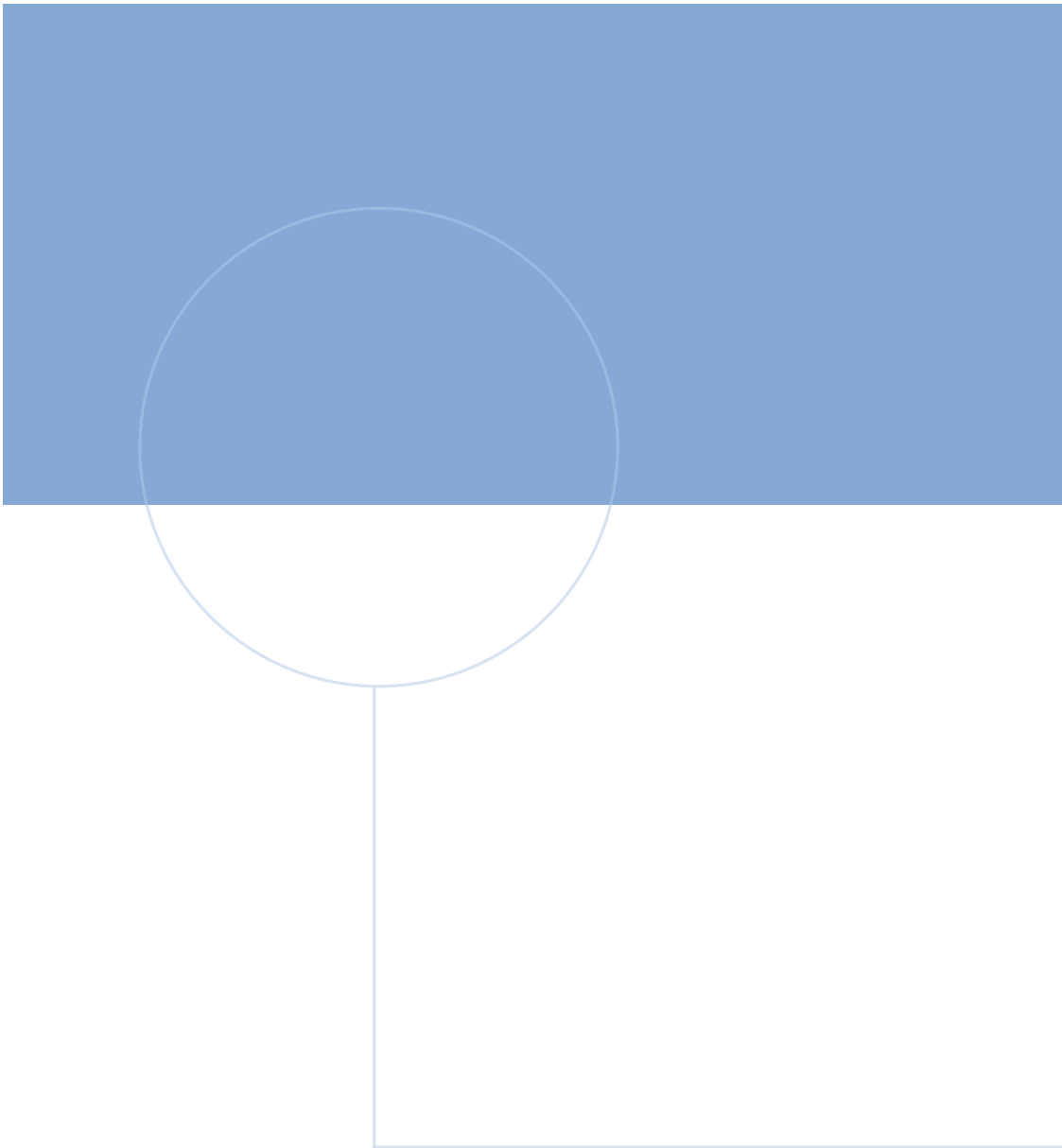

NTNU

Norwegian University of
Science and Technology